Simulated hydrological dynamics and coupled iron redox cycling impact methane production in an Arctic soil

Benjamin N. Sulman[1], Fengming Yuan[1], Teri O'Meara[1], Baohua Gu[1], Elizabeth Herndon[1], Jianqiu Zheng[3], Peter Thornton[1], and David E. Graham[2]

1. Climate Change Science Institute and Environmental Sciences Division, Oak Ridge National Laboratory
2. Biosciences Division, Oak Ridge National Laboratory
3. Biological Sciences Division, Pacific Northwest National Laboratory

Key Points:

- Ferric iron reduction can fuel decomposition in iron-rich Arctic soils. Higher rates of iron reduction reduce methane production
- We coupled iron and carbon cycling in a geochemical reaction model under simulated cycles of oxic and anoxic conditions
- Oxic-anoxic cycling in simulations reduced methane emissions and increased carbon dioxide production by regenerating oxidized iron

Abstract:

The fate of organic carbon (C) in permafrost soils is important to the climate system due to the large global stocks of permafrost C. Thawing permafrost can be subject to dynamic hydrology,

making redox processes an important factor controlling soil organic matter (SOM) decomposition rates and greenhouse gas production. In iron (Fe)-rich permafrost soils, Fe(III) can serve as a terminal electron acceptor, suppressing methane (CH_4) production and increasing carbon dioxide (CO_2) production. Current large-scale models of Arctic C cycling do not include Fe cycling or pH interactions. Here, we coupled Fe redox reactions and C cycling in a geochemical reaction model to simulate the interactions of SOM decomposition, Fe(III) reduction, pH dynamics, and greenhouse gas production in permafrost soils subject to dynamic hydrology. We evaluated the model using measured CO_2 and CH_4 fluxes as well as changes in pH, Fe(II), and dissolved organic C concentrations from oxic and anoxic incubations of permafrost soils from polygonal permafrost sites in northern Alaska, United States. In simulations of higher frequency oxic-anoxic cycles, rapid oxidation of Fe(II) to Fe(III) during oxic periods and gradual Fe(III) reduction during anoxic periods reduced cumulative CH_4 fluxes and increased cumulative CO_2 fluxes. Lower pH suppressed CH_4 fluxes through its direct impact on methanogenesis and by increasing Fe(III) bioavailability. Our results suggest that models that do not include Fe-redox reactions and its pH dependence could overestimate CH_4 production and underestimate CO_2 emissions and SOM decomposition rates in Fe-rich, frequently waterlogged Arctic soils.

Plain language summary

Soils in cold regions store large amounts of carbon that may be converted to climate-warming greenhouse gases as frozen soils thaw. Methane, a powerful greenhouse gas, is primarily produced when soils are flooded and lack oxygen. However, Arctic soils are also rich in iron, which some soil microorganisms can use instead of oxygen through a decomposition pathway that also produces carbon dioxide rather than methane. The computer models that are currently used to predict greenhouse gas emissions from thawing Arctic soils do not include iron interactions. We built a new model to simulate how iron, oxygen, and carbon interact in soils that are repeatedly flooded and drained. We tested the model using laboratory measurements of greenhouse gas production and iron cycling in Arctic soils. Our model simulations showed that when soils cycle more often between being flooded and exposed to air, iron is recycled to forms that can fuel carbon dioxide production while reducing methane gas production. Our results

suggest that including iron cycling in soil carbon models could improve predictions of the climate warming potential of greenhouse gas emissions from thawing Arctic soils.

1. Introduction

Permafrost regions contain enormous soil organic carbon (C) stocks (Hugelius et al., 2014). The fate of this vast C pool is critical to the global climate system because of the potential for decomposition of permafrost organic matter (OM) and C release into the atmosphere as greenhouse gases (Schuur et al., 2015; Turetsky et al., 2020). Because thawing permafrost often drives physical collapse and flooding, anoxic processes are an important component of permafrost OM decomposition. Major uncertainties in current understanding of permafrost thaw include the amount of C that will be mineralized and the relative amounts of CO_2 and CH_4 that will be produced by decomposition of OM in thawing permafrost soils.

Decomposition processes in saturated Arctic soils are tightly coupled to cycling of other elements including oxygen (O), nitrogen (N), and iron (Fe), which can serve as terminal electron acceptors (Dettling et al., 2006; Lipson et al., 2010). The presence of electron acceptors such as Fe(III) has been shown to suppress the production of CH_4, which provides a lower energy benefit to microbial metabolism, when Fe reducers are able to outcompete methanogens for substrates (Lipson et al., 2012; Miller et al., 2015). Simultaneous methanogenesis and ferric Fe (Fe(III)) reduction have been observed in Arctic soils, however, indicating that microbial processes do not necessarily strictly follow the redox ladder (Roy Chowdhury et al., 2015; Herndon et al., 2015; Yang et al., 2016; Reiche et al., 2008; Zheng et al., 2018). Many Arctic soils are rich in Fe(III)-bearing minerals and OM-bound Fe(III), and as a result, redox cycling of Fe can be an important control on OM degradation and C mineralization in permafrost soils (Herndon et al., 2017). Terminal electron acceptor availability and CH_4 production are also strongly dependent on soil pH (Zheng et al., 2019).

Despite the importance of such redox cycling processes for determining organic matter decomposition and greenhouse gas production in Arctic soils, the models applied at ecosystem to global scales to predict C cycling and related climate change feedbacks do not explicitly represent redox processes or pH dynamics (Wang et al., 2019; Wania et al., 2013; Xu et al., 2016). This omission opens the possibility that model projections could overestimate CH_4 emission and underestimate organic C mineralization and CO_2 production rates in soils where

alternate terminal electron acceptors are abundant. Such bias could be amplified in soils with dynamic hydrology that drives oscillations in redox conditions and consequent fluctuations in terminal electron acceptor variability.

Here, we simulated coupled OM decomposition and Fe redox cycling in the reactive transport model PFLOTRAN (Hammond et al., 2014). PFLOTRAN has been applied in biogeochemical contexts such as hyporheic zones (Dwivedi et al., 2018), and has previously been directly coupled to a land surface model and used to simulate soil organic matter cycling (Tang, Yuan, et al., 2016). We parameterized a biogeochemical reaction network using laboratory incubations of permafrost soils collected from different layers and microtopographic settings in a polygonal permafrost landscape, and then used the model to investigate how interactions between C and Fe cycling affect CH_4 and CO_2 production over oxic-anoxic cycles across a range of soil pH.

2. Methods

2.1. Model simulations

Simulations were conducted using a reaction network defined in PFLOTRAN (Figure 1, Table 1) building on reaction network developments from previous modeling studies using a different chemical reaction model, PHREEQC (Tang, Zheng, et al., 2016; Zheng et al., 2019) and previous implementation of soil organic matter decomposition reactions in PFLOTRAN (Tang, Yuan, et al., 2016). Organic matter pools in the reaction network included solid soil organic matter (SOM) and dissolved organic matter (DOM). Solid organic matter was first hydrolyzed to DOM, which could then be completely oxidized to CO_2 through aerobic decomposition (consuming O_2) or decomposed to produce organic acids (represented in the model by acetate) and CO_2 through fermentation (in anoxic conditions). Under anoxic conditions, acetate could be mineralized either by microbial reduction of Fe(III) or by acetoclastic methanogenesis. Aqueous Fe(III) ions were equilibrated with amorphous $Fe(OH)_3$ minerals through kinetic precipitation and dissolution reactions, which were calculated using Transition State Theory type rate laws (Dwivedi et al., 2018). These precipitation-dissolution relationships were highly pH dependent, with extremely low concentrations of uncomplexed aqueous Fe(III) ions under typical pH conditions. The model included equilibrium aqueous complexes of Fe(III) with DOM and

120 acetate, which greatly increased the concentration of total aqueous Fe(III). However, note that in
121 PFLOTRAN, aqueous chemical reaction rates, including Fe(III) reduction rates, are calculated
122 based on free ion concentrations rather than total aqueous concentrations. Fe(III) reduction
123 converted Fe(III) to more soluble ferrous Fe (Fe(II)) ions. Under oxic conditions, Fe(II) was
124 rapidly oxidized back to Fe(III), with the oxidation rate estimated using data from oxic
125 incubations (see Section 2.2). Fe(III) reduction and Fe(II) oxidation effectively functioned as
126 reductive dissolution and oxidative precipitation of $Fe(OH)_3$ due to the tight coupling between
127 the aqueous and mineral phases.
128 Methanogenesis was simulated as a combination of acetoclastic and hydrogenotrophic
129 pathways. pH dependence of the two methane pathways were determined based on an
130 optimization to measurements of Kotsyurbenko et al. (2007) (Figure S1). The optimized pH
131 dependence had the form:
132 $$F(pH) = \frac{10^{-pH}}{10^{-pH}+10^{-k_1}} \frac{10^{-k_2}}{10^{-pH}+10^{-k_2}} \quad (1)$$
133
134 Where $F(pH)$ is relative reaction rate as a function of pH for either methanogenesis pathway,
135 and k_1 and k_2 are parameters determining limitation by low and high pH, respectively. For
136 acetoclastic methanogenesis, the optimization found k_1 and k_2 both equal to 5.5. For
137 hydrogenotrophic methanogenesis, the optimization found $k_1 = 6.75$ and $k_2 < 0$, indicating no
138 limitation at low pH.
139 We conducted two sets of simulations representing alternative approaches to the
140 interaction between methanogenesis and Fe(III) reduction. In one set of simulations,
141 methanogenesis was directly inhibited by the presence of Fe(III) and O_2, which represented more
142 energetically favorable terminal electron acceptors. This approach assumes that simultaneous
143 Fe(III) reduction and methanogenesis is limited, which is consistent with the traditional redox
144 ladder conceptual model but may not be accurate for systems where simultaneous
145 methanogenesis and Fe(III) reduction are common as noted above. In the second approach, the
146 direct inhibition of methanogenesis by Fe(III) was removed, and methanogenesis was inhibited
147 only by O_2. SOM aerobic decomposition and anaerobic hydrolysis followed CLM-CN
148 decomposition kinetics (Tang, Yuan, et al., 2016) modified to allow Monod and inverse Monod
149 (inhibition) responses to aqueous chemical species and assuming no nitrogen limitation of

decomposition. Microbial aqueous reactions were assumed to follow multi-Monod kinetics of the form:

$$R = V_{max} \prod_N \frac{C_{S_N}}{K_{S_N} + C_{S_N}} \prod_M \frac{K_{I_M}}{K_{I_M} + C_{I_M}} \quad (2)$$

where R is reaction rate (mol (L H_2O)$^{-1}$ s^{-1}), V_{max} is maximum reaction rate (mol L^{-1} s^{-1}), N is the set of reactant species (including substrates and terminal electron acceptors), M is the set of inhibiting species, C_{S_N} is the concentration of the Nth substrate, K_{S_N} is the half-saturation constant of the Nth substrate, C_{I_M} is the concentration of the Mth inhibiting species, and K_{I_M} is the inhibition constant of the Mth inhibiting species.

In addition to the kinetic reactions described above, the reaction network included the pH buffering effect of soil organic matter. The soil matrix was assumed to contain surface complexation sites that could exchange H^+ ions under changing pH conditions. The volumetric density of these proton exchange sites was proportional to organic matter concentration in the soil layer being simulated (following Zheng et al., 2019) and the fraction of sorbed H^+ followed equilibrium sorption kinetics as defined in PFLOTRAN (https://www.pflotran.org/documentation/theory_guide/mode_reactive_transport.html).

Aerated and saturated conditions were simulated by varying the diffusion rate of O_2 between the simulated soil layer and a boundary condition representing aqueous O_2 concentration at equilibrium with the atmosphere. Flux was calculated based on the difference between O_2 concentration in the soil layer and in the boundary condition:

$$F_{O_2} = \left(\frac{[O_2]_{sat} - [O_2]_S}{\Delta z}\right) k_d \quad (3)$$

where F_{O_2} is flux rate of O_2 between the soil porewater and boundary condition (mol cm^{-2} s^{-1}), $[O_2]_{sat}$ is the aqueous O_2 concentration at saturation with respect to the atmosphere (mol cm^{-3}), $[O_2]_S$ is the soil aqueous O_2 content, Δz is the soil layer thickness (cm), and k_d is the diffusion coefficient (cm^2 s^{-1}). Under aerated conditions, k_d was set to 0.1 cm^2 s^{-1}, and under saturated conditions, k_d was set to zero, preventing O_2 from being replenished. For purposes of gas diffusion, Δz was assumed to be 10 cm. For simplicity, soil water content was assumed to be constant and equal to porosity across aerated and saturated conditions. This assumption prevented the model from simulating changes in aqueous concentrations driven only by differences in water content associated with drying.

180

181 Table 1: Porewater reactions included in the model. Monod and inhibition species are followed
182 by the half-saturation concentration (M, mol L^{-1}) in parentheses. DOM is expressed per mol C
183 and is assumed to have a stoichiometry 6 C:12 H:6 O.

Reaction	Stoichiometry	Reaction type	Reaction rate parameter (s^{-1} for SOM and M s^{-1} for Monod)	Monod species (half-saturation concentration [M])	Inhibition species (inhibition constant [M])
SOM hydrolysis	SOM-C + H_2O → DOM-C	SOM	$1.0x10^{-8}$		DOM (0.5)
Fermentation	DOM-C +0.33 H_2O → 0.33 CH_3COO^- + 0.33 CO_2^- + 0.33 H^+ + 0.67 H_2	Monod	$4.0x10^{-7}$	DOM-C (0.5)	Acetate (0.04) O_2 (10^{-5})
DOM aerobic respiration	DOM-C + O_2 → CO_2 + H_2O	Monod	$5.0x10^{-7}$	O_2 (10^{-4}) DOM-C (0.5)	
Acetate aerobic respiration	CH_3COO^- + 2 O_2 + H^+ → 2 CO_2 + 2 H_2O	Monod	$5.0x10^{-7}$	O_2 (10^{-4}) Acetate (0.04)	
Fe(III) reduction	CH_3COO^- + 8 Fe^{3+} + 2 H_2O → 2 CO_2 + 8 Fe^{2+} + 7 H^+	Monod	$3.0x10^{-8}$	Acetate (0.04) Fe(III) (10^{-10})	O_2 (10^{-5})

Fe(II) oxidation	$Fe^{2+} + 0.25\ O_2 + H^+ \rightarrow Fe^{3+} + 0.5\ H_2O$	Monod	$1.0x10^{-6}$	O_2 (10^{-4}) Fe(II) (0.1)	
Acetoclastic methanogenesis	$CH_3COO^- + H^+ \rightarrow CH_4 + CO_2$	Monod	$2.0x10^{-8}$	Acetate (0.04) H^+ ($10^{-5.5}$)	O_2 (10^{-5}) Fe(III) (10^{-10})** H^+ ($10^{-5.5}$)
Hydrogenotrophic methanogenesis	$4\ H_2 + CO_2 \rightarrow CH_4 + 2\ H_2O$	Monod	$9.6x10^{-9}$	H_2 (0.1) HCO_3^- (0.1)	O_2 (10^{-5}) Fe(III) (10^{-10})** H^+ ($10^{-6.75}$)
H_2 oxidation	$2\ H_2 + O_2 \rightarrow 2\ H_2O$	Monod	$1.0x10^{-6}$	H_2 (0.1) O_2 (10^{-4})	
$Fe(OH)_3$	$Fe(OH)_3 + 3\ H^+ \leftrightarrow Fe^{3+} + 3\ H_2O$	Precipitation-dissolution	$1.0x10^{-6}$ mol m^{-2} surface area s^{-1}		
*$Fe(OH)_3$ reductive dissolution	$Fe(OH)_3 + 0.125\ CH_3COO^- + 2.125\ H^+ \rightarrow 2.75\ H_2O + 0.25\ CO_2 + Fe^{2+}$				
*$Fe(OH)_3$ oxidative precipitation	$Fe^{2+} + 0.25\ O_2 + 2.5\ H_2O \rightarrow Fe(OH)_3 + 2\ H^+$				

*The $Fe(OH)_3$ reductive dissolution and oxidative precipitation equations are represented in the model through separate precipitation-dissolution and oxidation/reduction steps but the combined stoichiometries are shown here to ease interpretation of their effects on pH.

**Fe(III) inhibition terms for methanogenesis were included in one set of simulations and omitted in the other to test the impact of this assumption on simulation results.

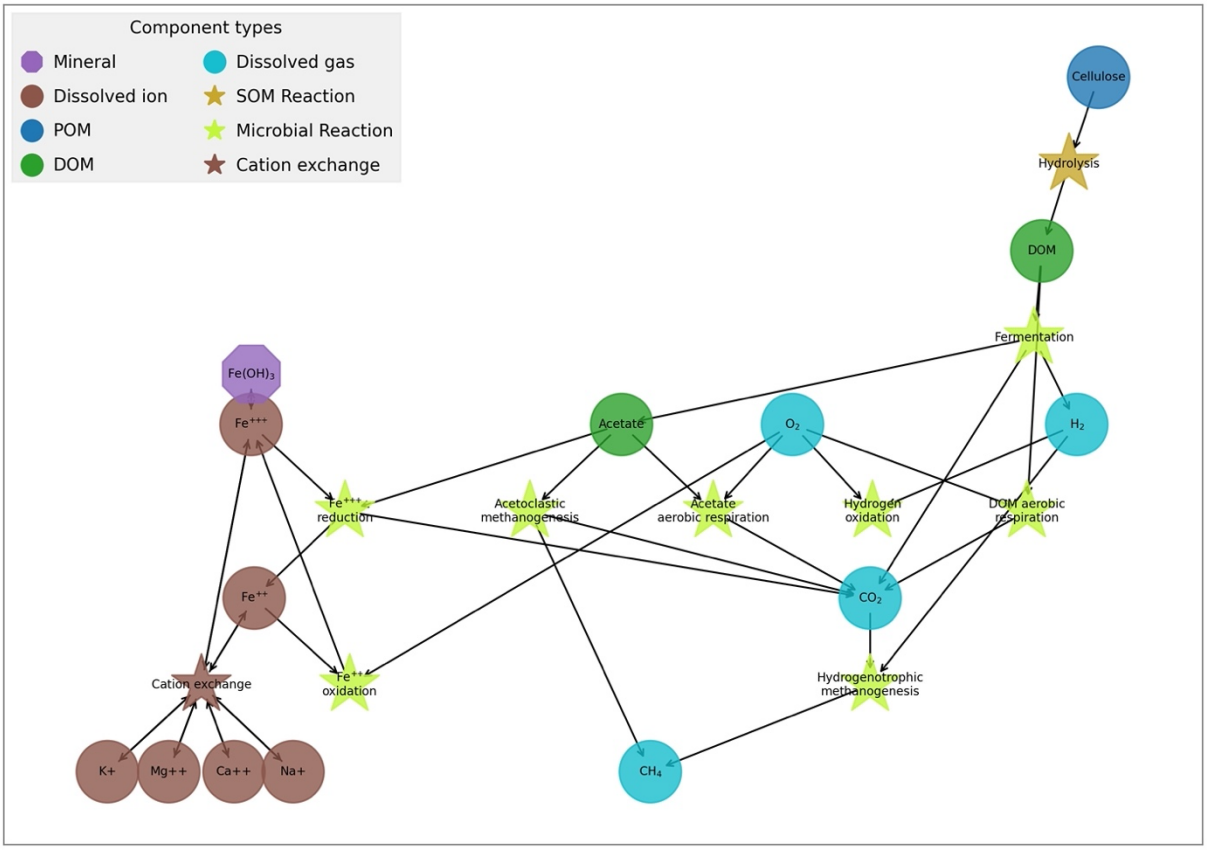

Figure 1: Network diagram of reactions included in the PFLOTRAN reaction network. Circles show chemical pools, and stars show reactions. Some chemical species, including H^+, are omitted for clarity.

2.2. Comparison with incubation measurements

Model simulations were parameterized using previously published measurements from laboratory microcosm incubations of seasonally thawed soil from the active layer of permafrost-underlain polygons (Figure 2; S5), as synthesized by Zheng et al. (2018, 2019) and porewater chemistry measurements from Herndon et al. (2016). Briefly, intact frozen soil cores were collected from Utqiagvik, Alaska and include trough, ridge, and center locations in ice-wedge polygons. Frozen soils were processed under anoxic conditions, and 15 g of soil from organic or mineral layers was used to establish triplicate microcosm incubations under anoxic conditions (N_2 headspace) or oxic conditions (air) (Zheng et al., 2018; Roy Chowdhury et al., 2015). Layers were distinguished by color and abundance of soil organic carbon. Incubations included an oxic

incubation of a high-centered polygon center organic horizon and anoxic incubations of organic and mineral horizons from a trough and a rim location. Head space CH_4 and CO_2 concentrations were measured using gas chromatography throughout the incubation period, and subsamples from separate microcosm incubations were used to determine changes in pH and exchangeable Fe(II) concentrations (Roy Chowdhury et al., 2015). Water extractable organic carbon was extracted from ground, freeze-dried soil, and low molecular weight organic acids were analyzed using ion chromatography (Herndon et al., 2015). Averages and standard errors over replicate incubation CO_2 and CH_4 flux measurements were used for comparison with modeled values at the appropriate time point. Reported standard errors of observed Fe(II) concentrations from Roy Chowdhury et al. (2015) and reported standard errors of water extractable organic carbon and total organic acids from Herndon et al. (2015) were used for comparisons with those quantities. Measurement uncertainties were not available for pH.

Model rate constants and key parameters were adjusted to maximize agreement (based on root mean square error (RMSE) and correlation coefficient (R)) between modeled and measured time series of CO_2 flux, CH_4 flux, pH, and concentrations of Fe(II), DOM, and organic acids (compared with acetate in the model) across four incubations with the multiple time points of the relevant measurements. Fermentation rate constant and half-saturation (K_S) for acetate were identified as particularly sensitive parameters, and simulations were conducted across a range of these parameters to identify the optimal values (Figs. S2 and S3). The same rate constants and half-saturation constants were applied to all horizons. Simulated incubations were initialized using available measurements from each incubation. SOC and bulk density were determined using measured SOC, assuming bulk density followed the relation of (Bockheim et al., 2003):

$$BD = e^{\frac{8.2432 - SOC(\%)}{9.7872}} \quad (4)$$

where SOC (%) is SOC in mass percentage and BD is bulk density in units of g cm^{-3}. Note that since measurements were expressed per unit dry soil mass, the lack of reported bulk density measurements means that any mismatch between actual and measured bulk density would introduce error to model-measurement comparisons.

Soil pH at the beginning of the simulated incubation was set as the measured pH at time zero of the incubation. Initial aqueous Fe(II) concentration was set as the measured aqueous Fe(II)

concentration at time zero, and initial Fe oxide mineral mass was set to 1.5 times the increase in measured Fe(II) concentration (per unit soil mass) over the course of the incubation, thereby assuming that two thirds of initial Fe oxides were reduced to Fe(II) over the course of each incubation. This correction was based on the assumption that some fraction of the Fe oxides were not reduced over the course of the incubations, likely representing crystalline oxides that are more resistant to microbial reduction, and aligned $Fe(OH)_3$ concentrations in the model with measurements of total extractable Fe relative to Fe(II) concentrations from similar soils (Herndon et al., 2017). Initial DOM and acetate concentrations were set using measured DOM and organic acid concentrations, respectively. Cation exchange capacity (CEC) was set using SOC content, assuming that CEC of organic matter was 200 meq $(100\ g)^{-1}$ and CEC of mineral material was 25 meq $(100\ g)^{-1}$ (Ping et al., 1998). Initial hydrolysable SOC was set using measured SOC, assuming that hydrolysable SOC represented 5% of total SOC (consistent with a small labile fraction; Schädel et al., 2013). Initial concentrations of Mg^{2+}, Ca^{2+}, Na^{+}, and K^{+} were set using mean porewater chemistry measurements from (Herndon et al., 2015, 2016).

2.3. Simulated oxic-anoxic cycling

Oxic-anoxic cycles were simulated by varying the k_d over time to represent transitions between aerated and saturated states. k_d was changed instantaneously at the time of transition between aerated and saturated conditions. Simulations were conducted over a 150-day period, beginning with a 15-day anoxic spinup period. 10% of the remaining simulation time was spent under aerated conditions to represent a wetland system that was periodically aerated but primarily under flooded conditions. Simulations with only one cycle were aerated for 15 days at the end of the 15-day spinup period and then remained under anoxic conditions for the remainder of the simulation. Simulations with multiple cycles shortened the length of each aerated period so that the total time under aerated and saturated conditions was the same (15 days under aerated conditions) in all simulations. The effect of pH was tested by repeating simulations with initial pH conditions ranging in increments of 0.5 from 4.5 to 6.0, a range typical of Arctic tundra soils. These simulations were set up for mineral and organic horizons from the permafrost polygon trough location using the same data sources and initialization approach described above.

3. Results

3.1. Comparison of model simulations and incubations

Model simulations correlated well with observations for Fe(II) concentrations, pH, and DOM concentration (Figure 2). Simulated acetate concentrations were not as well correlated with total organic acid measurements, particularly later in the incubations. Simulated CO_2 production was overestimated by the model for the polygon rim organic horizon (squares on Fig. 2e), while other incubations were more accurately simulated. This overestimation may have been due to the high organic content (39%) and consequently low calculated bulk density (0.28 g cm^{-3}) of polygon rim organic horizon, which meant that fluxes expressed on a per-weight basis were divided by a small mass. Note that the model simulated cumulative production of CO_2 and CH_4 in porewater and did not explicitly simulate transport of dissolved gases across the soil surface to the head space. CH_4 production was also overestimated for organic horizons but was well correlated between model and observations for mineral horizons (Fig. 2c,d). Including direct inhibition of CH_4 production by Fe(III) lowered organic horizon CH_4 fluxes early in the incubations, which increased overall correlation between model and observations (Fig. 2d). In the oxic incubation of the center organic horizon, the model simulated a very rapid decline in Fe(II) concentrations as Fe(II) was rapidly oxidized to Fe(III) (Fig. 2a). The model did not reproduce the higher Fe(II) concentration observed later in the oxic incubation. The model reproduced measured increases in pH during the Fe(III) reduction phase in the trough cores but not in the rim cores.

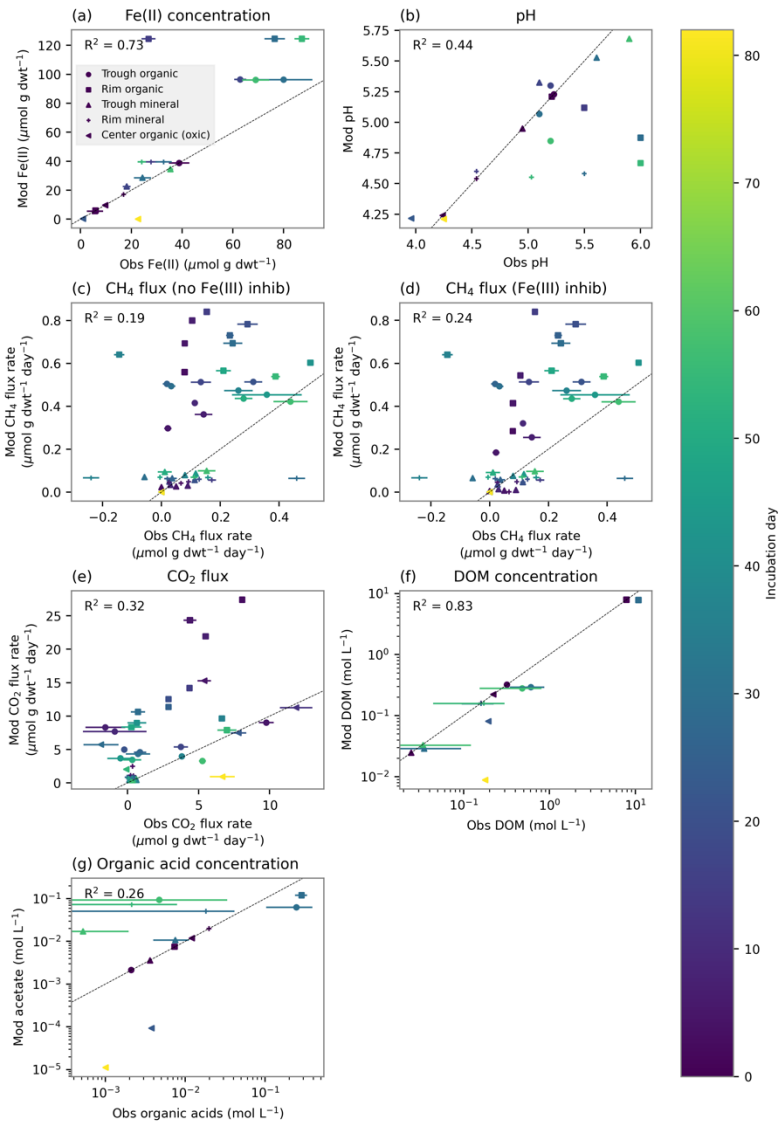

Figure 2: Comparisons between incubation measurements and model simulations. Measurements (Zheng et al., 2018, 2019) are shown on the horizontal axis and corresponding simulated values are shown on the vertical axis. The dotted line shows a 1-1 relationship. Symbol colors indicate day of the incubation, with lighter colors occurring later in the incubation. Symbols show permafrost polygon setting of the incubation source material (trough, rim, or oxic center) and soil horizon (organic or mineral). Coefficient of determination (R^2) between modeled and measured points is show on each panel. Panel (c) shows CH_4 flux from simulations without direct inhibition of methanogenesis by Fe(III), and panel (d) shows CH_4 flux from simulations including direct inhibition. Only CH_4 flux is shown for both configurations because the other quantities were not visually different between configurations.

295

296 ## 3.2. Simulations of oxic-anoxic cycles

297 Simulations of repeated oxic-anoxic cycles highlighted the succession of decomposition phases
298 as the system depleted different terminal electron acceptors, as well as the interaction of these
299 phases with pH (Fig. 3, S4). During oxic periods, CO_2 fluxes were high, supported by abundant
300 oxygen (Fig. 3b). During anoxic periods, O_2 was rapidly depleted, causing a sharp decline in
301 CO_2 production rate. Early in each anoxic period, Fe(III) reduction increased quickly, as shown
302 by the production rate of Fe(II) ions (Fig. 3c). Fe(III) reduction depleted Fe oxide minerals (Fig.
303 3d) and increased pH (Fig. 3e) due to the net proton consumption effect of $Fe(OH)_3$ reductive
304 dissolution (Table 1). CH_4 fluxes (Fig 3a) were inhibited by Fe(III), delaying the increase in CH_4
305 production rates under anoxic conditions. Fe(III) reduction produced twice as much CO_2 per unit
306 acetate consumed as methanogenesis and had a faster reaction rate, causing CO_2 production to be
307 higher during the Fe(III) reduction phase than during the methanogenesis phase. The temporal
308 pattern of Fe(III) reduction and its effect on methanogenesis were controlled by a combination of
309 Fe(III) accessibility and pH. Under lower pH conditions (dotted lines), Fe oxide mineral
310 solubility was higher, leading to higher Fe(III) availability and consequently more rapid Fe(III)
311 reduction rates and stronger inhibition of methanogenesis. Rapid Fe(III) reduction at pH of 5.0
312 was consistent with high observed accumulation rates of Fe(II) in incubations starting at pH of
313 around 5 (Fig. S5). Under higher pH conditions (solid and dashed lines), the lowered Fe oxide
314 solubility, combined with the rise in pH driven by Fe oxide dissolution, inhibited further Fe(III)
315 reduction. Rising pH allowed methanogenesis rates to increase over time in simulated mineral
316 horizons (Fig. 3) while methanogenesis rates increased after depletion of soluble Fe oxides in
317 simulated organic horizons (Fig. S4). The effect of including direct inhibition of methanogenesis
318 by Fe(III) was most apparent in CH_4 fluxes, which were lower overall and increased more slowly
319 when direct inhibition was included (Fig. 3a). In simulations with the lowest initial pH and direct
320 inhibition, CH_4 production did not begin until iron oxides had been depleted. However, the
321 general pattern of increasing CH_4 production over time during anoxic periods was evident in
322 simulations with or without direct inhibition.
323

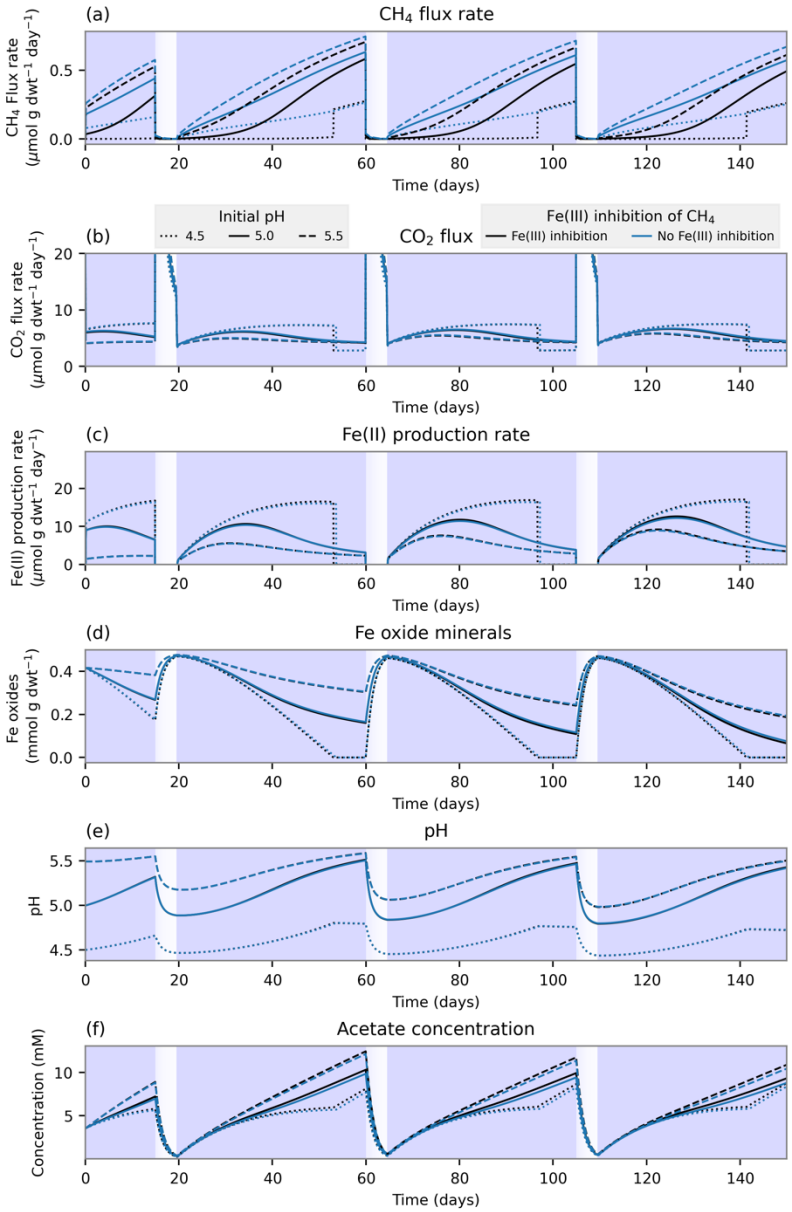

Figure 3: Simulated oxic-anoxic cycles for a mineral horizon. Blue backgrounds indicate anoxic conditions and white backgrounds indicate oxic conditions. Black lines show simulations with direct inhibition of methanogenesis by Fe(III) and blue lines show simulations without direct inhibition (a): CH_4 flux rate. (b): CO_2 flux rate. (c): Fe(II) production rate via Fe(III) reduction. (d): Fe oxide mineral concentration. (e): pH. (f): Acetate concentration.

Integrating CO_2 and CH_4 fluxes across multiple oxic-anoxic cycles showed the cumulative impact of the Fe-C-pH interactions on CO_2 and CH_4 fluxes (Fig. 4). Integrated CO_2 fluxes increased with more oxic-anoxic cycles, with a stronger increase in the simulated organic than in

the simulated mineral horizon (Fig. 4a). Cumulative CO_2 fluxes were minimally affected by pH and were not sensitive to whether the simulation included direct inhibition of CH_4 production by Fe(III). The total increase in cumulative CO_2 production from one to five cycles was approximately 1.9 mmol g dwt^{-1} (a 120% increase relative to one cycle) in the organic horizon and 0.52 mmol g dwt^{-1} (a 100% increase) in the mineral horizon.

Cumulative CH_4 production declined with increasing numbers of oxic-anoxic cycles. At pH of 6, CH_4 fluxes from the organic horizon declined from 0.12 to 0.09 mmol g dwt^{-1} (25%) between one and five cycles, and at pH of 4.5 integrated CH_4 fluxes declined from 0.047 to 0.035 mmol g dwt^{-1} (26%). In the mineral horizon, CH_4 flux declined from 0.08 to 0.03 mmol g dwt^{-1} (62%) at pH of 6.0 and from 0.03 to < 0.01 mmol g dwt^{-1} at pH of 4.5. Note that while the fractional changes in CH_4 fluxes were comparable with the fractional changes in CO_2 fluxes, the magnitude of C flux change was an order of magnitude higher for CO_2 than for CH_4.

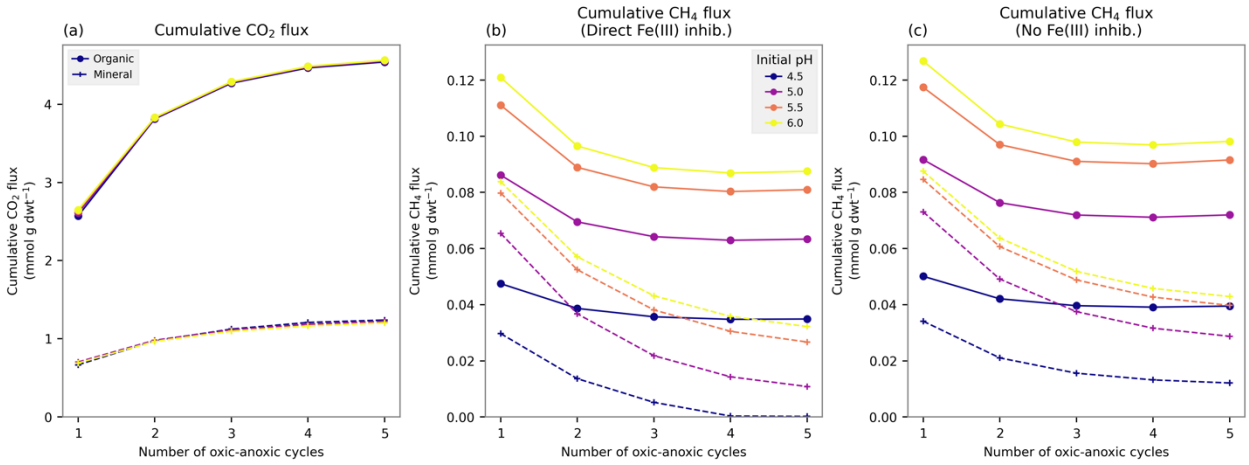

Figure 4: Integrated CO_2 and CH_4 fluxes over a 150-day period with varying pH and number of oxic-anoxic cycles. Each simulation had a total of 15 days of oxic conditions, divided evenly across the oxic-anoxic cycles. pH is indicated by symbol colors. Solid lines and circles show a simulated organic horizon; dashed lines and pluses show a simulated mineral horizon. (a): CO_2 flux. (b): CH_4 flux.

4. Discussion

4.1. Implications for model projections of Arctic carbon cycling

Current Earth system models omit redox interactions such as Fe-C coupling in simulations of SOM degradation, CO_2 emissions, and CH_4 production (Wania et al., 2013). Most models

simulate CH_4 production as a function of soil respiration, water content, and temperature. Our results suggest that models omitting redox processes such as Fe-C interactions could substantially overestimate CH_4 production and underestimate both CO_2 production and SOM decomposition in soils subject to water table fluctuations, particularly under acidic pH conditions. Our simulations confirm previous findings that Fe cycling under oxic and anoxic conditions driven by water table variation is an important driver of permafrost C cycling (Lipson et al., 2012) as well as C cycling in other wetland systems such as rice paddies (Kögel-Knabner et al., 2010; Yao et al., 1999). One model, CLM4Me (Riley et al., 2011), does include a parameterization of depletion of alternative terminal electron acceptors, which is simulated as a delayed increase in CH_4 production rate with a characteristic time scale of 30 days. While incorporating a temporal delay between the onset of anoxic conditions and maximum CH_4 production can partially mitigate overestimates of CH_4 production, such models depend on simplified parameterizations of the delay length and cannot easily accommodate the effects of variations in pH and Fe availability in different soils. Our results suggest that both the length and the strength of CH_4 emission suppression depend strongly on pH and the availability and solubility of Fe(III) oxide minerals (Fig. 3).

Thermodynamic calculations support the potential for increased Fe(III) reduction at low pH (Flynn et al., 2014; Bethke et al., 2011), although the available energy of the electron donating half-reaction (e.g., acetate oxidation) decreases as pH declines. The overall metabolic rate of Fe(III) reduction depends on both factors, making the rate's pH response sensitive to the soil chemical context and likely variable across soil types. Significant rates of Fe(III) reduction under low pH conditions are consistent with previous observations such as significant Fe(II) accumulation at $pH < 4.5$ in a northern peatland (Ye et al., 2012) and increased conversion of reducible iron to soluble forms at lower pH in paddy soils (Gotoh and Patrick, 1974). There is also evidence that Fe(III) reduction in normally alkaline paddy soils can be suppressed under low pH conditions; however, iron reduction proceeded rapidly in acidic paddy soils incubated under similar pH conditions (Jia et al., 2015). A biological dependence on pH was not included in our model structure, as we did not find sufficient quantitative evidence to support adding an additional pH dependence term of microbial Fe(III) reduction to the model at this time. Our results are consistent with previous model simulations of permafrost biogeochemical dynamics, which have highlighted the importance of pH buffering capacity (Tang, Zheng, et al., 2016;

Zheng et al., 2019). Our simulations extend previous model applications by simulating fluctuations in oxygen availability which serve as proxies for hydrological transitions. Furthermore, our simulations use a model with an existing interface to a full-featured land surface model (Tang, Yuan, et al., 2016), providing a pathway toward integrating detailed biogeochemical dynamics into large-scale model simulations.

Thawing permafrost undergoes substantial changes in hydrology that can drive varying biogeochemical processes, including flooding of collapsed permafrost (Turetsky et al., 2020) and drying of deeper thawed soil layers under warming (Pegoraro et al., 2020). While projections of how hydrology of permafrost itself will change are a grand challenge for predicting the future of Arctic systems (Walvoord & Kurylyk, 2016), the impacts of hydrological changes on biogeochemical cycles represent their own set of challenges for predictive modeling. Hydrological changes driven by permafrost thaw can drive rapid organic matter losses (O'Donnell et al., 2012) and increases in CO_2 and CH_4 emissions (Natali et al., 2015). The complex and rapidly-changing hydrological patterns in thawing permafrost systems can drive dynamic water tables that make predictions of biogeochemical cycling particularly challenging, but emerging hydrological model frameworks are allowing more accurate simulations of permafrost hydrology (Jan et al., 2018; Painter et al., 2013). Our biogeochemical model framework builds the groundwork for coupling next-generation hydrological simulations to biogeochemical dynamics for improved simulation of biogeochemical cycling in thawing permafrost.

4.2. Factors not considered

Our simulations did not explicitly include the role of organic matter sorption onto reactive Fe oxide surfaces as a stabilization process for soil carbon. Both stabilization of OM through sorption and destabilization of sorbed OM by dissolution of iron oxides under anoxic conditions have been recently highlighted as important components of permafrost soil C cycling (Opfergelt, 2020; Patzner et al., 2020). While the focus of the present study was on short-term CH_4 and CO_2 production rather than SOC stabilization processes, the explicit representation of Fe oxide mineral precipitation and dissolution processes and their dependence on pH and redox conditions makes this model framework well suited to incorporating SOC stabilization effects of Fe oxides in the future. The assumption that Fe(III) reduction occurs in the aqueous phase may also ignore

418 the role of direct microbial interactions with Fe oxide mineral surfaces and formation of biofilms
419 (Roden and Zachara, 1996), does not allow explicit treatment of Fe(III) reduction from
420 organically complexed Fe(III) species, and omits the diverse set of strategies that microbial
421 Fe(III) reducers can use to access solid iron oxides as electron acceptors (Kappler et al., 2021).
422 These omissions could bias the model with respect to Fe(III) reduction under circumneutral pH
423 since direct reduction of solid-phase Fe-oxide can occur, allowing Fe(III) reduction to continue
424 but with different forms of Fe(III) being reduced. Including additional Fe oxide phases beyond
425 $Fe(OH)_3$ could also allow more exploration of how variations in mineral properties such as
426 specific surface area and solubility affect coupled Fe-C cycling. Soil humic acids, such as
427 quinones, are not considered as terminal electron acceptors here. Similarly, the present model
428 does not include nutrient cycling, but would be well suited to represent N cycle processes such as
429 nitrification and denitrification as well as the role of Fe oxides in sequestering phosphorus in
430 Arctic soils (Herndon et al., 2019; Herndon et al., 2020). This model also does not account for
431 microbial biomass production and maintenance, which assimilates a portion of reduced substrate
432 and nutrients, releasing oxidized products.
433 Our model simulations tested alternative assumptions with respect to the inhibition of
434 methanogenesis by Fe(III) availability. In one approach, methanogenesis was directly inhibited
435 by Fe(III). This is consistent with the redox ladder conceptual model, and with studies finding
436 suppression of methanogenesis following Fe(III) additions (Reiche et al., 2008; Miller et al.,
437 2015), but may not adequately reproduce previous observations of positive correlations between
438 Fe(III) reduction and methanogenesis (Herndon et al., 2015; Yang et al., 2016). The alternative
439 approach relaxed this assumption, allowing simultaneous Fe(III) reduction and methanogenesis.
440 The direct inhibition approach did reduce simulated CH_4 production, especially in the early
441 stages following a transition from oxic to anoxic conditions (Fig. 3a) as well as lowering
442 cumulative CH_4 production over multiple cycles for both organic and mineral soils (Fig. 4b,c).
443 However, the qualitative dependence on pH and oxic/anoxic cycling was similar for both
444 approaches, and fit between model and observations was only slightly different between the two
445 approaches (Fig. 1). The similar outcomes are likely due to the role of pH, which has a strong
446 impact on methanogenesis and responded to Fe(III) reduction similarly in both approaches (Fig.
447 3e), as well as the depletion of substrates by more rapid Fe(III) reduction (Fig. 3f) which in turn
448 reduced methanogenesis even without direct inhibition (Lovely, 1991). Overall, we conclude that

direct inhibition of methanogenesis by Fe(III) availability was not necessary for the model to represent key Fe-C interactions.

Our simulations focused on a single soil layer and did not include vertical variations in soil properties or vertical transport of gases such as O_2, CO_2, or CH_4. Thus, they omitted potentially important effects such as water table fluctuations and methanotrophy. Aerobic methanotrophy reduces net methane fluxes in oxic and suboxic layers, while anaerobic methane oxidiation can slowly remove methane in anoxic layers. The oxic-anoxic cycles in the current model could be viewed as a time-for-space substitution approach for characterizing soil transition zones close to a dynamic water table. A vertically resolved model would allow more realistic simulations of how the key Fe-C interactions we identified act across vertical oxic-anoxic transitions in soils. More explicit vertically resolved simulations are planned as a next step with this model framework. Future applications of the model that include transport and vertical interactions, will make direct comparisons with field measurements more straightforward.

5. Conclusions

We developed a biogeochemical model framework to represent interactions among carbon, Fe, and pH dynamics in Arctic soils. The model reproduced CO_2 and CH_4 emission patterns along with pH and Fe redox dynamics from oxic and anoxic soil microcosm incubations. Simulations of repeated oxic-anoxic cycles showed that Fe(III) reduction could suppress CH_4 but enhance CO_2 production when oxic-anoxic cycles were more frequent, as the reduced Fe(II) was oxidized during oxic periods and served as a preferential electron acceptor at the beginning of each anoxic period. The effects of Fe on CO_2 and CH_4 emissions were stronger under lower pH conditions. Our results suggest that models that omit Fe and other terminal electron acceptors as well as pH dynamics could overestimate CH_4 production and underestimate CO_2 production in systems with dynamic water tables, and that site-specific chemical factors including pH, bulk density, and Fe availability may be necessary for improved simulations of C cycle dynamics and greenhouse gas emissions from hydrologically dynamic Arctic soils.

Acknowledgements:

The NGEE Arctic project is supported by the Office of Biological and Environmental Research in the US Department of Energy's Office of Science. This research used resources of the Compute and Data Environment for Science (CADES) at the Oak Ridge National Laboratory, which is supported by the Office of Science of the U.S. Department of Energy under Contract No. DE-AC05-00OR22725. JZ is supported by COMPASS-FME, a multi-institutional project supported by the U.S. Department of Energy, Office of Science, Biological and Environmental Research as part of the Environmental System Science Program. The Pacific Northwest National Laboratory is operated for DOE by Battelle Memorial Institute under contract DE-AC05-76RL01830. Thanks to Erin Berns for helpful comments on the manuscript.

Data availability:

Model code, output data, and analysis scripts are archived in the NGEE Arctic Data Repository [doi:10.5440/1814844; Sulman et al., 2021].

6. References

Bethke, C. M., Sanford, R. A., Kirk, M. F., Jin, Q., & Flynn, T. M. (2011). The thermodynamic ladder in geomicrobiology. *American Journal of Science*, *311*(3), 183–210. https://doi.org/10.2475/03.2011.01

Bockheim, J. G., Hinkel, K. M., & Nelson, F. E. (2003). Predicting carbon storage in tundra soils of Arctic Alaska. *Soil Science Society of America Journal*, *67*(3), 948–950.

Dettling, M. D., Yavitt, J. B., & Zinder, S. H. (2006). Control of organic carbon mineralization by alternative electron acceptors in four peatlands, central New York state, USA. *Wetlands*, *26*(4), 917–927. https://doi.org/10.1672/0277-5212(2006)26[917:COOCMB]2.0.CO;2

Dwivedi, D., Arora, B., Steefel, C. I., Dafflon, B., & Versteeg, R. (2018). Hot Spots and Hot Moments of Nitrogen in a Riparian Corridor. *Water Resources Research*, *54*(1), 205–222. https://doi.org/10.1002/2017WR022346

Flynn, T. M., O'Loughlin, E. J., Mishra, B., DiChristina, T. J., & Kemner, K. M. (2014). Sulfur-mediated electron shuttling during bacterial iron reduction. *Science*, *344*(6187), 1039–1042. https://doi.org/10.1126/science.1252066

Gotoh, S., & Patrick, W. H. (1974). Transformation of Iron in a Waterlogged Soil as Influenced

by Redox Potential and pH. *Soil Science Society of America Journal. Soil Science Society of America*, *38*(1), 66–71. https://doi.org/10.2136/sssaj1974.03615995003800010024x

Hammond, G. E., Lichtner, P. C., & Mills, R. T. (2014). Evaluating the performance of parallel subsurface simulators: An illustrative example with PFLOTRAN. *Water Resources Research*, *50*(1), 208–228. https://doi.org/10.1002/2012WR013483

Herndon, E. M., Yang, Z., Bargar, J., Janot, N., Regier, T. Z., Graham, D. E., et al. (2015). Geochemical drivers of organic matter decomposition in Arctic tundra soils. *Biogeochemistry*, *126*(3), 397–414. https://doi.org/10.1007/s10533-015-0165-5

Herndon, E. M., Yang, Z., Graham, D. E., Wullschleger, S. D., Gu, B., & Liang, L. (2016). Surface and Active Layer Pore Water Chemistry from Ice Wedge Polygons, Barrow, Alaska, 2013-2014. Oak Ridge, TN: Next Generation Ecosystem Experiments Arctic Data Collection, Oak Ridge National Laboratory. https://doi.org/10.5440/1226245

Herndon, E. M., AlBashaireh, A., Singer, D., Roy Chowdhury, T., Gu, B., & Graham, D. (2017). Influence of iron redox cycling on organo-mineral associations in Arctic tundra soil. *Geochimica et Cosmochimica Acta*, *207*, 210–231. https://doi.org/10.1016/j.gca.2017.02.034

Herndon, E. M., Kinsman-Costello, L., Duroe, K. A., Mills, J., Kane, E. S., Sebestyen, S. D., et al. (2019). Iron (oxyhydr)oxides serve as phosphate traps in tundra and boreal peat soils. *Journal of Geophysical Research: Biogeosciences*. https://doi.org/10.1029/2018JG004776

Herndon, E., Kinsman-Costello, L., Di Domenico, N., Duroe, K., Barczok, M., Smith, C., & Wullschleger, S. D. (2020). Iron and iron-bound phosphate accumulate in surface soils of ice-wedge polygons in arctic tundra. *Environmental Science. Processes & Impacts*, *22*(7), 1475–1490. https://doi.org/10.1039/d0em00142b

Hugelius, G., Strauss, J., Zubrzycki, S., Harden, J. W., Schuur, E. A. G., Ping, C. L., et al. (2014). Estimated stocks of circumpolar permafrost carbon with quantified uncertainty ranges and identified data gaps. *Biogeosciences*, *11*(23), 6573–6593. https://doi.org/10.5194/bg-11-6573-2014

Jan, A., Coon, E. T., Painter, S. L., Garimella, R., & Moulton, J. D. (2018). An intermediate-scale model for thermal hydrology in low-relief permafrost-affected landscapes. *Computational Geosciences*, *22*(1), 163–177. https://doi.org/10.1007/s10596-017-9679-3

539 Jia, R., Li, L.-N., & Qu, D. (2015). pH shift-mediated dehydrogenation and hydrogen production
540 are responsible for microbial iron(III) reduction in submerged paddy soils. *Journal of Soils*
541 *and Sediments*, *15*(5), 1178–1190. https://doi.org/10.1007/s11368-015-1084-8
542 Kappler, A., Bryce, C., Mansor, M., Lueder, U., Byrne, J. M., & Swanner, E. D. (2021). An
543 evolving view on biogeochemical cycling of iron. *Nature Reviews. Microbiology*, *19*(6),
544 360–374. https://doi.org/10.1038/s41579-020-00502-7
545 Kögel-Knabner, I., Amelung, W., Cao, Z., Fiedler, S., Frenzel, P., Jahn, R., et al. (2010).
546 Biogeochemistry of paddy soils. *Geoderma*, *157*(1), 1–14.
547 https://doi.org/10.1016/j.geoderma.2010.03.009
548 Kotsyurbenko, O. R., M. W. Friedrich, M. V. Simankova, A. N. Nozhevnikova, P. N. Golyshin,
549 K. N. Timmis, and R. Conrad (2007). Shift from Acetoclastic to H_2-Dependent
550 Methanogenesis in a West Siberian Peat Bog at Low pH Values and Isolation of an
551 Acidophilic Methanobacterium Strain. *Applied and Environmental Microbiology* 73 (7):
552 2344–48. https://doi.org/10.1128/AEM.02413-06.
553 Lipson, D. A., Jha, M., Raab, T. K., & Oechel, W. C. (2010). Reduction of iron (III) and humic
554 substances plays a major role in anaerobic respiration in an Arctic peat soil. *Journal of*
555 *Geophysical Research: Biogeosciences*, *115*(4), 1–13.
556 https://doi.org/10.1029/2009JG001147
557 Lipson, D. A., Zona, D., Raab, T. K., Bozzolo, F., Mauritz, M., & Oechel, W. C. (2012). Water-
558 table height and microtopography control biogeochemical cycling in an Arctic coastal
559 tundra ecosystem. *Biogeosciences*, *9*(1), 577–591.
560 Lovley, D. R. (1991). Dissimilatory Fe(III) and Mn(IV) reduction. *Microbiological Reviews*,
561 *55*(2), 259–287. https://doi.org/10.1128/mr.55.2.259-287.1991
562 Miller, K. E., Lai, C.-T., Friedman, E. S., Angenent, L. T., & Lipson, D. A. (2015). Methane
563 suppression by iron and humic acids in soils of the Arctic Coastal Plain. *Soil Biology &*
564 *Biochemistry*, *83*, 176–183. https://doi.org/10.1016/j.soilbio.2015.01.022
565 Natali, S. M., Schuur, E. A. G., Mauritz, M., Schade, J. D., Celis, G., Crummer, K. G., et al.
566 (2015). Permafrost thaw and soil moisture driving CO_2 and CH_4 release from upland tundra.
567 *Journal of Geophysical Research: Biogeosciences*, *120*(3), 525–537.
568 https://doi.org/10.1002/2014JG002872
569 O'Donnell, Jonathan A., M. Torre Jorgenson, Jennifer W. Harden, A. David McGuire, Mikhail

570 Z. Kanevskiy, and Kimberly P. Wickland. 2012. The Effects of Permafrost Thaw on Soil
571 Hydrologic, Thermal, and Carbon Dynamics in an Alaskan Peatland. *Ecosystems* 15 (2):
572 213–29. https://doi.org/10.1007/s10021-011-9504-0.
573 Opfergelt, S. (2020). The next generation of climate model should account for the evolution of
574 mineral-organic interactions with permafrost thaw. *Environmental Research Letters*, *15*(9).
575 https://doi.org/10.1088/1748-9326/ab9a6d
576 Painter, S. L., Moulton, J. D., & Wilson, C. J. (2013). Modeling challenges for predicting
577 hydrologic response to degrading permafrost. *Hydrogeology Journal*, *21*(1), 221–224.
578 https://doi.org/10.1007/s10040-012-0917-4
579 Patzner, M. S., Mueller, C. W., Malusova, M., Baur, M., Nikeleit, V., Scholten, T., et al. (2020).
580 Iron mineral dissolution releases iron and associated organic carbon during permafrost thaw.
581 *Nature Communications*, *11*(1), 6329. https://doi.org/10.1038/s41467-020-20102-6
582 Pegoraro, E. F., Mauritz, M. E., Ogle, K., Ebert, C. H., & Schuur, E. A. G. (2020). Lower soil
583 moisture and deep soil temperatures in thermokarst features increase old soil carbon loss
584 after 10 years of experimental permafrost warming. *Global Change Biology*, gcb.15481.
585 https://doi.org/10.1111/gcb.15481
586 Ping, C. L., Bockheim, J. G., Kimble, J. M., Michaelson, G. J., & Walker, D. A. (1998).
587 Characteristics of cryogenic soils along a latitudinal transect in arctic Alaska. *Journal of*
588 *Geophysical Research*, *103*(D22), 28917–28928. https://doi.org/10.1029/98jd02024
589 Reiche, M., Torburg, G., & Küsel, K. (2008). Competition of Fe(III) reduction and
590 methanogenesis in an acidic fen. *FEMS Microbiology Ecology*, *65*(1), 88–101.
591 https://doi.org/10.1111/j.1574-6941.2008.00523.x
592 Riley, W. J., Subin, Z. M., Lawrence, D. M., Swenson, S. C., Torn, M. S., Meng, L., et al.
593 (2011). Barriers to predicting changes in global terrestrial methane fluxes: analyses using
594 CLM4Me, a methane biogeochemistry model integrated in CESM. *Biogeosciences*, *8*(7),
595 1925–1953. https://doi.org/10.5194/bg-8-1925-2011
596 Roden, E. E., & Zachara, J. M. (1996). Microbial Reduction of Crystalline Iron(III) Oxides:
597 Influence of Oxide Surface Area and Potential for Cell Growth. *Environmental Science &*
598 *Technology*, *30*(5), 1618–1628. https://doi.org/10.1021/es9506216
599 Roy Chowdhury, T., Herndon, E. M., Phelps, T. J., Elias, D. A., Gu, B., Liang, L., et al. (2015).
600 Stoichiometry and temperature sensitivity of methanogenesis and CO2 production from

saturated polygonal tundra in Barrow, Alaska. *Global Change Biology*, *21*(2), 722–737. https://doi.org/10.1111/gcb.12762

Schädel, C., Luo, Y., David Evans, R., Fei, S., & Schaeffer, S. M. (2013). Separating soil CO2 efflux into C-pool-specific decay rates via inverse analysis of soil incubation data. *Oecologia*, *171*(3), 721–732. https://doi.org/10.1007/s00442-012-2577-4

Schuur, E. A. G., McGuire, A. D., Schädel, C., Grosse, G., Harden, J. W., Hayes, D. J., et al. (2015). Climate change and the permafrost carbon feedback. *Nature*, *520*(7546), 171–179. https://doi.org/10.1038/nature14338

Sulman, B. N., Yuan, F., O'Meara, T., Graham, D., Gu, B., Herndon, H., Zheng, J. 2021. Iron cycle interactions with hydrological dynamics reduce methane production in a simulated Arctic soil: Modeling Archive. Next Generation Ecosystem Experiments Arctic Data Collection, Oak Ridge National Laboratory, U.S. Department of Energy, Oak Ridge, Tennessee, USA. https://doi.org/10.5440/1814844.

Tang, G., Yuan, F., Bisht, G., Hammond, G. E., Lichtner, P. C., Kumar, J., et al. (2016). Addressing numerical challenges in introducing a reactive transport code into a land surface model: A biogeochemical modeling proof-of-concept with CLM-PFLOTRAN 1.0. *Geoscientific Model Development*, *9*(3), 927–946. https://doi.org/10.5194/gmd-9-927-2016

Tang, G., Zheng, J., Xu, X., Yang, Z., Graham, D. E., Gu, B., et al. (2016). Biogeochemical modeling of CO2 and CH4 production in anoxic Arctic soil microcosms. *Biogeosciences*, *13*(17), 5021–5041. https://doi.org/10.5194/bg-13-5021-2016.

Throckmorton, H. M., Heikoop, J. M., Newman, B. D., Altmann, G. L., Conrad, M. S., Muss, J. D., et al. (2015). Pathways and transformations of dissolved methane and dissolved inorganic carbon in Arctic tundra watersheds: Evidence from analysis of stable isotopes. *Global Biogeochemical Cycles*, *29*(11), 1893–1910. https://doi.org/10.1002/2014GB005044

Turetsky, M. R., Abbott, B. W., Jones, M. C., Anthony, K. W., Olefeldt, D., Schuur, E. A. G., et al. (2020). Carbon release through abrupt permafrost thaw. *Nature Geoscience*, *13*(2), 138–143. https://doi.org/10.1038/s41561-019-0526-0

Walvoord, M. A., & Kurylyk, B. L. (2016). Hydrologic Impacts of Thawing Permafrost-A Review. *Vadose Zone Journal*, *15*(6), vzj2016.01.0010. https://doi.org/10.2136/vzj2016.01.0010

Wang, Y., Yuan, F., Yuan, F., Gu, B., Hahn, M. S., Torn, M. S., et al. (2019). Mechanistic

Modeling of Microtopographic Impacts on CO2 and CH4 Fluxes in an Alaskan Tundra Ecosystem Using the CLM-Microbe Model. *Journal of Advances in Modeling Earth Systems*, *11*(12), 4288–4304. https://doi.org/10.1029/2019MS001771

Wania, R., Melton, J. R., Hodson, E. L., Poulter, B., Ringeval, B., Spahni, R., et al. (2013). Present state of global wetland extent and wetland methane modelling: Methodology of a model inter-comparison project (WETCHIMP). *Geoscientific Model Development*, *6*(3), 617–641. https://doi.org/10.5194/gmd-6-617-2013

Xu, X., Yuan, F., Hanson, P. J., Wullschleger, S. D., Thornton, P. E., Riley, W. J., et al. (2016). Reviews and syntheses: Four decades of modeling methane cycling in terrestrial ecosystems. *Biogeosciences*, *13*(12), 3735–3755. https://doi.org/10.5194/bg-13-3735-2016

Yang, Z., Wullschleger, S. D., Liang, L., Graham, D. E., & Gu, B. (2016). Effects of warming on the degradation and production of low-molecular-weight labile organic carbon in an Arctic tundra soil. *Soil Biology & Biochemistry*, *95*, 202–211. https://doi.org/10.1016/j.soilbio.2015.12.022

Yao, H., Conrad, R., Wassmann, R., & Neue, H. U. (1999). Effect of soil characteristics on sequential reduction and methane production in sixteen rice paddy soils from China, the Philippines, and Italy. *Biogeochemistry*, *47*(3), 269–295. https://doi.org/10.1007/BF00992910

Ye, R., Jin, Q., Bohannan, B., Keller, J. K., McAllister, S. A., & Bridgham, S. D. (2012). pH controls over anaerobic carbon mineralization, the efficiency of methane production, and methanogenic pathways in peatlands across an ombrotrophic–minerotrophic gradient. *Soil Biology & Biochemistry*, *54*, 36–47. https://doi.org/10.1016/j.soilbio.2012.05.015

Zheng, J., RoyChowdhury, T., Herndon, E. M., Yang, Z., Gu, B., Wullschleger, S., & Graham, D. (2018). Synthesis of Soil Geochemical Characteristics and Organic Carbon Degradation from Arctic Polygon Tundra, Barrow, Alaska. Oak Ridge, TN: Next Generation Ecosystem Experiments Arctic Data Collection, Oak Ridge National Laboratory. https://doi.org/10.5440/1440029

Zheng, J., RoyChowdhury, T., Yang, Z., Gu, B., Wullschleger, S. D., & Graham, D. E. (2018). Impacts of temperature and soil characteristics on methane production and oxidation in Arctic tundra. *Biogeosciences* , *15*(21), 6621–6635. https://doi.org/10.5194/bg-15-6621-2018

Zheng, J., Thornton, P. E., Painter, S. L., Gu, B., Wullschleger, S. D., & Graham, D. E. (2019). Modeling anaerobic soil organic carbon decomposition in Arctic polygon tundra: insights into soil geochemical influences on carbon mineralization. *Biogeosciences*, *16*(3), 663–680. https://doi.org/10.5194/bg-16-663-2019